Available online at www.sciencedirect.com
SCIENCE DIRECT®
Journal of Nuclear Materials 347 (2005) 52–68
journal of nuclear materials
www.elsevier.com/locate/jnucmat

An ATEM study of oxidation behavior of SCC crack tips in 304L stainless steel in high temperature oxygenated water

Y.H. Lu [a,b,*], Q.J. Peng [a], T. Sato [a], T. Shoji [a]

[a] *Fracture Research Institute, Graduate School of Engineering, Tohoku University, Aramaki Aoba 01, Aoba-ku, Sendai City 980-8579, Japan*
[b] *Department of Materials Physics, Beijing University of Science and Technology, Beijing 100083, PR China*

Received 22 July 2004; accepted 12 July 2005

Abstract

Oxidation behavior at the tips of several stress corrosion cracking (SCC) crack, including intergranular SCC (IGSCC) and transgranular SCC (TGSCC) cracks, in heat-treated 304L stainless steel in high temperature oxygenated water was studied using a field emission gun-analytical transmission electron microscopy (FEG–ATEM). These SCC cracks were produced during SCC tests in two different heat-treated 304L stainless steels in high temperature pure water with two different levels of dissolved oxygen (DO). The study showed that oxygen played a key role in nucleation and propagation of SCC cracks. For the IGSCC crack, oxidation took place followed by nucleation and growth of microcracks in the oxide ahead of the crack tip on the grain boundary plane. The IGSCC crack then propagated by linkage with these microcracks. Oxides formed in the high temperature water with different DO had different configurations and microstructures. In the case of low DO, separate oxides of Cr_2O_3 and Fe_3O_4 types were formed, while the oxide formed in high DO consisted of mixed $FeCr_2O_4$ and Fe_3O_4. For the TGSCC crack, oxidation along deformation bands and nucleation and growth of microcracks within oxide were important mechanisms. It was found that Si was preferentially oxidized ahead of the crack tip, promoting SCC crack propagation. Ni enrichment at some SCC crack tips was also revealed.

PACS: 28.41.Qb; 46.50.+a; 61.72.Mm; 62.20.Mk; 68.37.Lp; 82.45.Bb

1. Introduction

Irradiation assisted stress corrosion cracking (IASCC) in both boiling water reactors (BWRs) and pressurized water reactors (PWRs) has been extensively studied in the last 30 years. The general pattern of IASCC is that the non-sensitized austenitic stainless steel (SS) becomes susceptible to intergranular failure when neutron fluence increases [1]. It is generally accepted that the main cracking mechanism and material cause for IASCC in the light water reactor (LWR) environment are film rupture/slip oxidation (dissolution) along radiation-induced Cr-depleted grain boundaries although IASCC is also affected by other mechanisms such as hydrogen embrittlement, radiation hardening, or enrichment of minor detrimental elements [2]. Usually IASCC

* Corresponding author. Address: Department of Materials Physics, Beijing University of Science and Technology, Beijing 100083, PR China.
E-mail address: lu_yonghao@yahoo.com.cn (Y.H. Lu).

0022-3115/$ - see front matter © 2005 Elsevier B.V. All rights reserved.
doi:10.1016/j.jnucmat.2005.07.006

occurs more easily in oxygenated water in BWR than in deoxygenated water in PWR [3–5]. However, several facts, for example cracking of cladding and baffle plate bolts under non-oxidizing potential, and some experimental results are proved to be contrary to expectations based on the Cr-depletion mechanism. For example, susceptibility to PWR-irradiated components to IASCC has been shown clearly from SSRT test in PWR simulated water although PWR water chemistry falls well within the range of protective electrochemical potential [1]. Further more, although it is clear that any depletion of Cr can induce an intergranular crack, it is not clear whether the Cr depletion or the Cr level itself is controlling this process [6]. In addition, the role of grain boundary segregation of minor alloying elements such as Si, P and S appears to be not well established, and sometimes contrary to general IASCC mechanism. The results of Jenssen et al. [4] show that a high-purity heat (low Si, S and P) of type 304 SS has similar IASCC susceptibility to a commercial purity one in BWR. However, the study of Jacobs et al. [7] shows the commercial heat is more susceptible to cracking in PWR and BWR, which is related to the higher level of silicon at the grain boundary in the commercial heat. Other researchers, for example Li et al. [8] and Yonezawa et al. [9], also observed that Si significantly affected the environmentally assisted corrosion (EAC) behavior of the simulated grain boundary (GB) steels by promoting intergranualr cracking in PWR. For P and S, it seems that their segregations have a little effect on promoting environmental cracking in high temperature water [10,11]. Obviously, the real basic mechanisms of IASCC nucleation and propagation are very critical to understand the above phenomena.

Up to now, the real basic mechanisms of nucleation and propagation of IASCC, especially of intergranular SCC (IGSCC), remain debate and need to be further investigated. Obviously, direct observation and examination of IGSCC crack tip and the corresponding microstructures in detail using analytical transmission electron microscopy (ATEM) method are a good way to gain insight into the mechanism of IGSCC crack. In this respect Thomas et al. [12–14] have first studied the IG attack regions and stress corrosion cracks in alloy 600 U-bend sample tested in 330 °C PWR water and irradiated 304 SS using ATEM technique, and conclude that an active-path dissolution or oxidation process is responsible for the IG attack and the SCC. Nevertheless, more works are needed to clarify this mechanism in different test conditions and different materials, for example, the widely-used 304L stainless steel tested in BWR.

In our project, the SCC crack tips in heat-treated 304L SS compact tension (CT) samples formed at different dissolved oxygen (DO) in 288 °C high temperature water were chosen to be analyzed by ATEM. The reason why the sensitized materials used is that Cr depletion formed during heat-treatment can be designed to simulate radiation induced segregation (RIS) effect. In this study, effects of oxygen, Cr depletion and Ni, Si enrichment at grain boundary on IGSCC were focused.

2. Experimental procedure

2.1. Materials and test conditions

Two 1-in. thick CT (1T-CT) specimens, named as CT-1 and CT-2, were fabricated from heat-treated 304L SS. The chemical composition of the materials is listed in Table 1.

Different heat-treatment processes were applied to the two specimens. The heat-treatment process of CT-1 was 650 °C × 100 h + air-cooling + 620 °C × 100 h + air-cooling, and that of CT-2 was 650 °C × 100 h + air-cooling + 550 °C × 100 h + air-cooling, followed by a warm rolling at 200–250 °C. The room-temperature mechanical properties of the two samples after such heat-treatments are also listed in Table 1. As can be seen, CT-2 has a high yield strength because of warm rolling. After heat treatment the microstructure and composition of grain boundaries were examined using a field emission gun (FEG) HF-2000 TEM equipped with a Voyager energy dispersion system (EDS). Fig. 1 shows the grain boundary morphology in the CT-1 sample. Obviously, as a result of such a long time heat-treatment, very low-density dislocations within grains and precipitation of a series of carbides along grain boundaries can be found. These carbides have considerable different shapes, and vary from several nanometers to several hundred nanometers in size, as shown in the corresponding dark field image (Fig. 1(b)). The grain boundary is also found to become curve because of existence of these carbides. The EDS analysis was performed between the carbides. Fig. 2 shows the concentration profiles for Cr, Ni and Fe in CT-1 sample.

Table 1
Chemical compositions (Fe balance) mechanical properties (room-temperature) of materials used in this study (wt%)

Materials	C	Si	Mn	P	S	Cr	Ni	Yield strength (MPa)	Tensile strength (MPa)	Elongation (%)
CT-1	0.012	0.69	1.46	0.005	0.006	18.55	12.08	228	517	62
CT-2								683	737	24

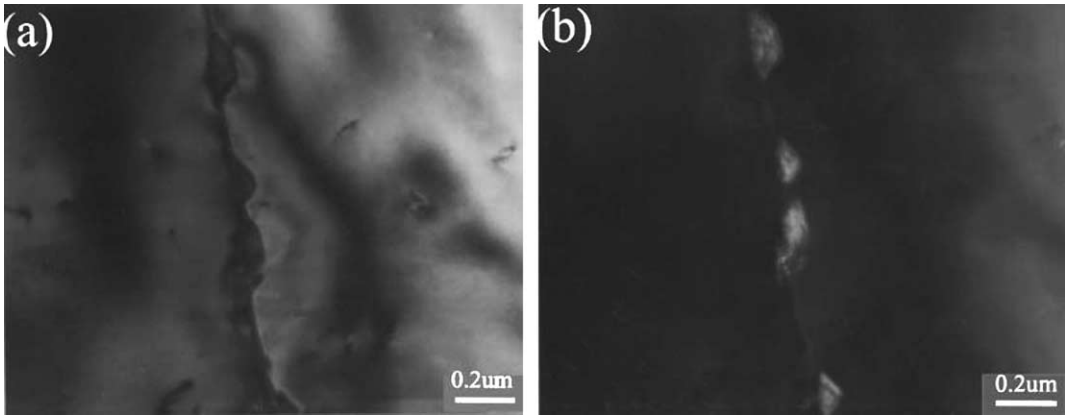

Fig. 1. (a) Bright and (b) dark field images of grain boundaries in CT-1 sample.

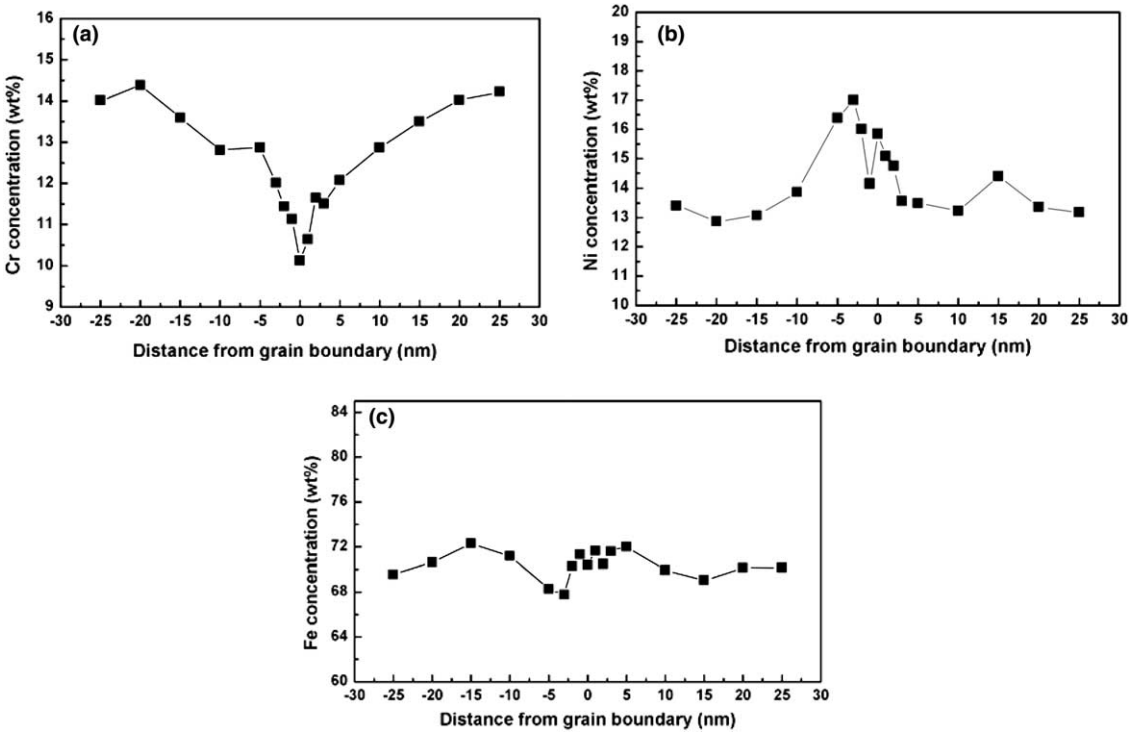

Fig. 2. (a) Cr, (b) Ni and (c) Fe profiles near a random grain boundary in CT-1 sample.

It can be found that Cr concentration falls down to about 10 wt%, which is about 8 wt% lower than that in matrix. However, Ni shows somewhat enrichment at the grain boundary, its concentration is about 16 wt% compared to about 12 wt% in the matrix. No obvious Fe concentration is found. The grain boundary morphology and elemental concentrations in sample CT-2 show no distinct difference with those in sample CT-1, except that after warm-rolling, the carbides distributed along the grain boundary look a little strip-like, whose TEM morphology is not shown in this paper.

SCC tests on each 1 T-CT specimen were performed in simulated BWR water with two different DO. Before the SCC test, both 1T-CT specimens were precracked in air by fatigue and then 5% side grooved on each side. The detailed environmental parameters for both tests

Table 2
Test conditions in BWR autoclave

Samples	Temperatures (°C)	D.O. (inlet) (ppm)	Conductivity (outlet) (S/cm)	Pressure (MPa)	Extension rate (m/s)
CT-1	288	>20	0.3 μ	8.4	5.9×10^{-9}
CT-2	288	2	0.06 μ	8.5	–

are listed in Table 2. Different loading modes were employed for the two tests. For the test under high DO of >20 ppm on the CT-1 specimen, slow strain rate tension (SSRT) was used to produce SCC. A schematic of loading mode used for the CT-2 specimen under low DO of 2 ppm is shown in Fig. 3. As can be seen, a triangular wave loading with different R (ratio of minimum to maximum loads) values was first applied to the specimen in order to transform the crack growth from transgranular to intergranular. Then a trapezoidal wave loading with the R value of 0.7 and a holding time of 3 h was applied to promote IGSCC.

After testing, a FEG Hitachi 4300 scanning electron microscopy (SEM) was used to examine both the side view and the fracture photography of the SCC crack tip. The corresponding images of SCC crack formed in CT-1 sample are shown in Fig. 4(a) and (b), respectively. Obviously the SCC crack is composed of several IGSCC and transgranular SCC (TGSCC) cracks as marked shown in Fig. 4(a). Correspondingly, the fractography consisting of intergranular and transgranular facets is found in the zone of SCC crack propagation, as shown in the middle of Fig. 4(b). SCC crack formed in CT-2 sample has a similar characterization.

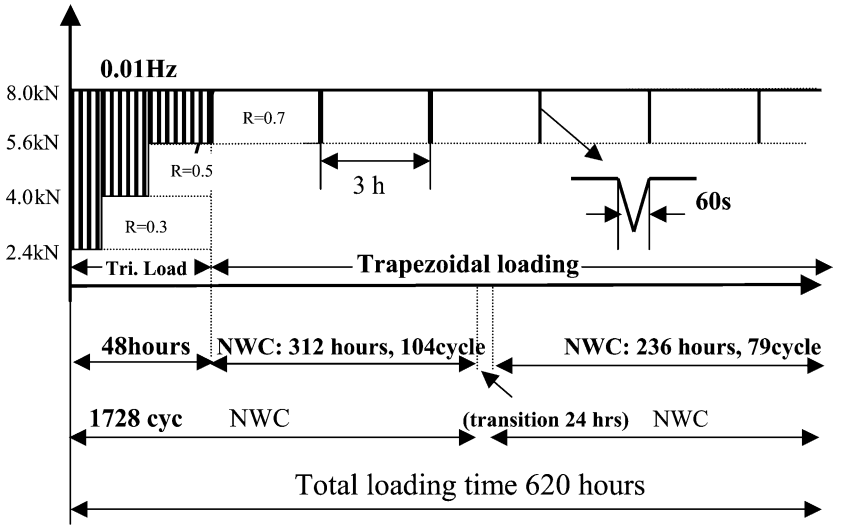

Fig. 3. The mode of applied stress for pre-crack and SCC test in CT-2 sample.

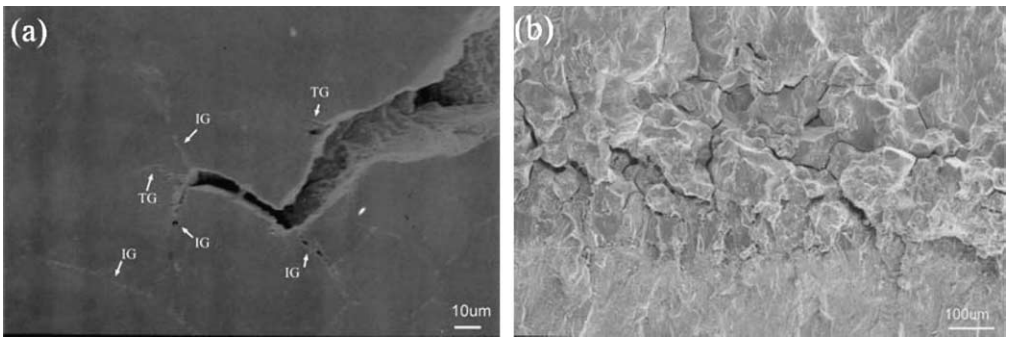

Fig. 4. SEM images of (a) SCC cracks and (b) the corresponding fractography of CT-1 sample tested in high DO water.

2.2. Preparation procedures of TEM specimens

The preparation of TEM cross section samples containing SCC crack tip was in accordance with Thomas's method [12]. The principle steps are summarized as follows:

(a) polishing the CT specimen surface and cut a foursquare column containing the SCC crack tip;
(b) polishing four side planes of foursquare column, and decrease the cross-sectional size to about 2×2 mm^2,
(c) inserting this foursquare column into a stainless steel tube about 3 mm in out diameter,
(d) slicing the foursquare column to thin slice about 0.5 mm in thickness using diamond cutter,
(e) mechanically polishing two surfaces of thin slice, and decreasing the thickness to about 100 μm,
(f) further thinning the slice using a Gatan Model 656 dimple grind, and decreasing thickness to about 20 μm,
(g) further thinning the slice using a Fischone Model 3000 dual ion miller until a hole was performed to make a TEM sample,
(h) thinning the TEM sample using ion-milling until a suitable SCC crack tip was found under TEM.

The thin slice was first ion-milled with 5 keV Ar ions at a beam current of 5.0 mA per gun with an incident angle of 15°. The sample-stage temperature maintained about 35 °C during ion-milling. After a hole was performed, the cyclic procedures including the ion-milling thinning at 2.5 keV/2.5 mA and with an incident angle of 10° and sequentially TEM observations were carried out until a suitable location was transparent under the TEM.

The observation of crack tip was examined using a FEG HF-2000 TEM equipped with a Voyager EDS system. During TEM analysis, the Fresnel image technique was widely used. Fresnel imaging is a phase contrast mechanism by which adjacent focus condition, fine structures of different refractive index appear in strong contrast under out-of-focus condition but disappear in-focus image.

3. Results

3.1. CT-2 specimen, low DO pure water

Fig. 5(a) shows an IGSCC crack tip in CT-2 specimen formed in 288 °C pure water with a low DO under a trapezoidal wave loading, which deflects from one grain boundary to another. The diffraction patterns on both sides of the crack tip shown in Fig. 5(b) indicate that this grain boundary is not a special one. The high-magnification image of Fig. 5(a) is shown in Fig. 5(c), from which an oxide wall filled completely the crack tip can be found along the IGSCC crack. Several microcracks are found to form within this oxide wall. An obvious and clear metal/oxide interface can also be seen. The high-magnification images of zones C and D at crack tip zone are shown in Fig. 6(a) and (b), respectively. Within the oxide many string type microcracks about 1 nm wide with various lengths can be seen distributed unevenly, nevertheless mainly lay parallel to the grain boundary (or the IGSCC crack tip). These string type microcracks played an important role in propagation of SCC crack. They nucleated, propagated and enclosed, forming a large one. The high-magnification image of part E in Fig. 5(c) is shown in Fig. 6(c), from which a lot of string type microcracks are found within the oxide. Similar to above observations, these string type microcracks also distribute unevenly. It is worthy of notice that no microcrack nucleates along the metal/oxide interface, indicating that the interface has a relatively high cohesive strength. Some high-density dislocations/faults within the metal matrix terminating at the metal/oxide interface indicate that a strong plastic deformation took place during SCC testing. In order to further study the interaction between oxide and grain boundary, the grain boundary was tilted about 40° by a rotation axis parallel to the grain boundary. Fig. 7(a) and (b) show the grain boundary before and after tilting respectively. Obviously the thickness of oxide becomes smaller after tilting. Although the grain boundary could not be tilted to an edge-on orientation because of limitation of TEM, it is also rational to deduce that the oxide and microcracks formed on the grain boundary plane. The microdiffraction patterns taken from points A and B in Fig. 5(c) with 5 nm beam size in diameter are shown in Fig. 5(d) and (e), respectively. Analysis of these diffraction patterns demonstrates that two different types of oxides formed during SCC test. The oxide at position A exhibits nanocrystalline, while the one at position B is crystalline. In fact, in the most positions, the diffraction patterns show the same characterization as that shown in Fig. 5(d). Fig. 6(d) is an example showing the interface of two types of oxides. The dark field image of the IGSCC crack using part of diffraction rings of oxide A in Fig. 5(e) is shown in Fig. 8(a) (overall morphology) and Fig. 8(b) (high-magnification image). In Fig. 8, two types of oxides with separate configurations are found within the oxide wall. Observing the front part of the crack demonstrates that the oxide wall becomes narrower on the grain boundary plane with penetration to deep grain boundary, indicating that oxygen diffusion was a gradual process along grain boundaries. When the oxygen partial pressure ahead of the crack tip reached a critical value enough for oxidation, oxidation took place there, and then oxide filled the crack tip. At last, the

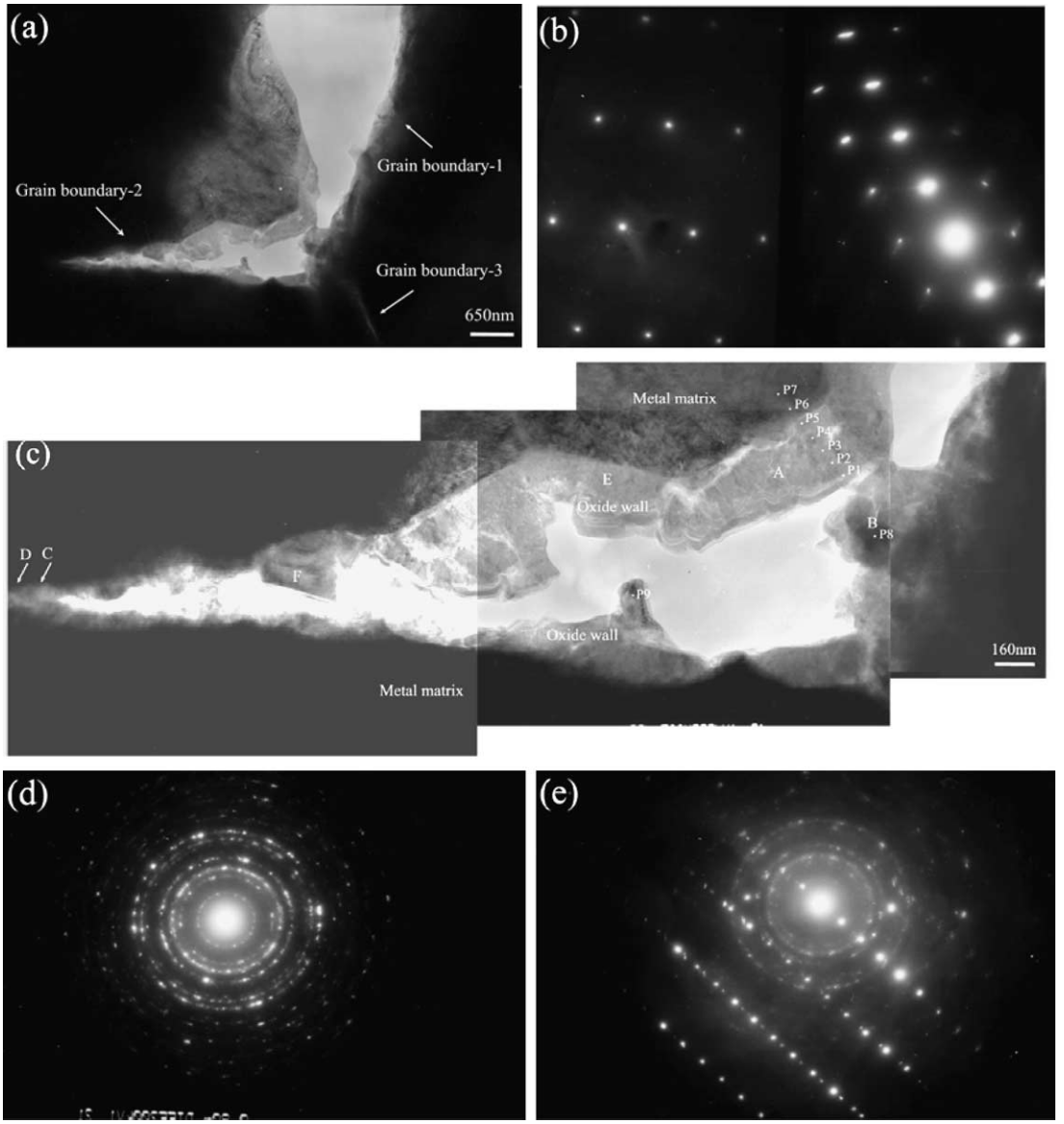

Fig. 5. (a) An IGSCC crack tip in CT-2 sample tested in low DO water, (b) the corresponding diffraction patterns of grains on both sides, and (c) the high-magnification image with the diffraction patterns at positions (d) A and (e) B.

microcracks nucleated within oxides and linked to the main SCC crack, leading to propagation of the SCC crack.

Further direct analyses of the oxides shown in Fig. 5(c) were conducted by EDS technique. During EDS analyses the probe beam size was focused to 1–2 nm in diameter according to analysis requirements. The analysis results of several typical positions marked in Fig. 5(c) are listed in Table 3, while the result for points P1–P7 in Fig. 5(c) is shown in Fig. 9, in which the position of metal/oxide interface is labeled. The analysis results of points P8 and P9 within another type of oxide are also listed in Table 3. Fig. 9 shows that, for most positions in Fig. 5, Cr content is higher than that in the metal matrix, while Fe and Ni contents are much lower. This implies that a Cr-rich oxide formed in most positions of the oxide film although it consists of the all presented elements. On the other hand, a few positions in Fig. 5 show the formation of Fe-rich oxide. In Fe-rich oxide, Cr content is much lower, while the Fe content is relatively higher. Analyses of the diffraction patterns of Cr-rich and Fe-rich oxides as shown in Fig. 5(d) and (e) indicates that the Cr-rich oxide is Cr_2O_3 type, and the Fe-rich oxide is Fe_3O_4 type.

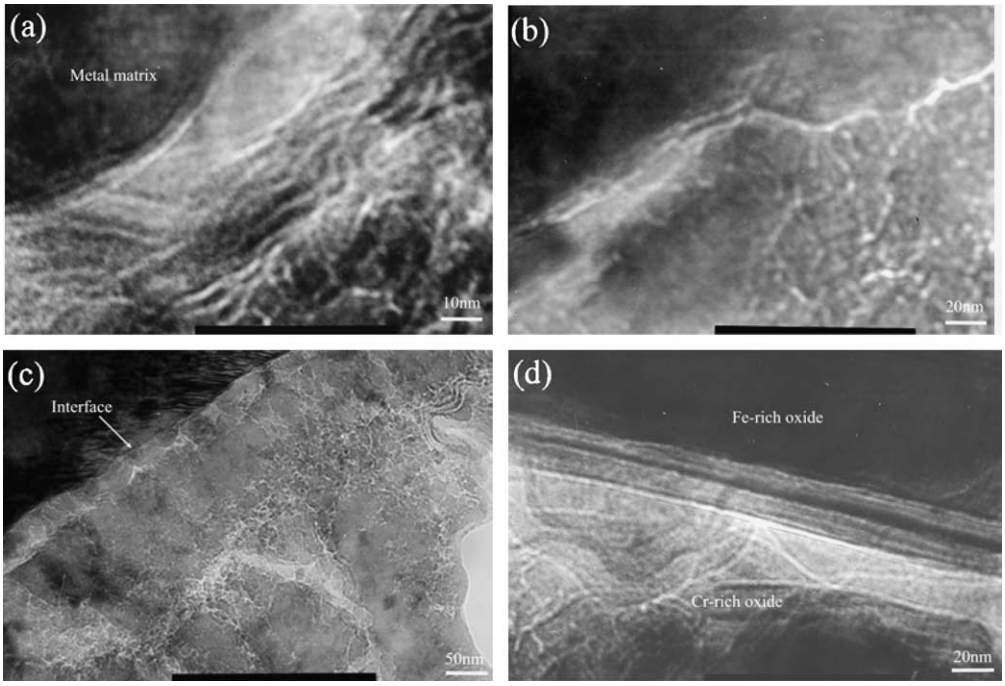

Fig. 6. High-magnification images of zones (a) C, (b) D, (c) E, and (d) F in Fig. 5(c).

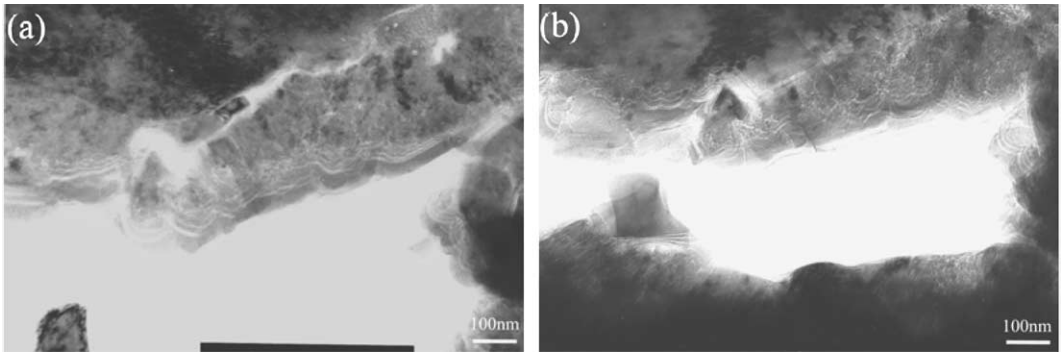

Fig. 7. TEM photographies of zone A in Fig. 5(a) before and (b) after its tilting about 40° by rotation axis parallel to grain boundary.

A transgranular SCC crack tip and its high-magnification image are shown in Fig. 10(a) and (b) respectively. It can be seen that a band type oxide first forms before the crack tip starts propagation. Results of EDS analyses of some positions around the crack tip as labeled in Fig. 10(b) are shown in Fig. 10(c) and (d). The result shows that the oxygen content in the band type oxide is much lower than that in the oxide at the grain boundary, indicating that the diffusion of oxygen is more difficult within the grain lattice. It is worthy of notice here that the Ni enrichment is found adjacent to crack tip. The Ni content is the highest at the crack tip, and decreases gradually with increasing the distance from the crack tip.

Fig. 11 shows an IGSCC crack tip, where the Ni enrichment is also found adjacent to it. It can be observed from Fig. 11(a) that an IGSCC crack tip propagates along the interface between the metal matrix and a strip with Ni enrichment that has been proved by EDS analysis (see Fig. 11(a)). Table 4 lists the results of the EDS analyses on some chosen positions as labeled in Fig. 11(b), which shows the oxygen enrichment in both Ni-rich strips and the adjacent zones. It is obvious that the Ni-rich strips form along the grain boundary, and the interface between the strips and matrix has lower fracture strength, resulting in propagation of the SCC crack tip along the interface.

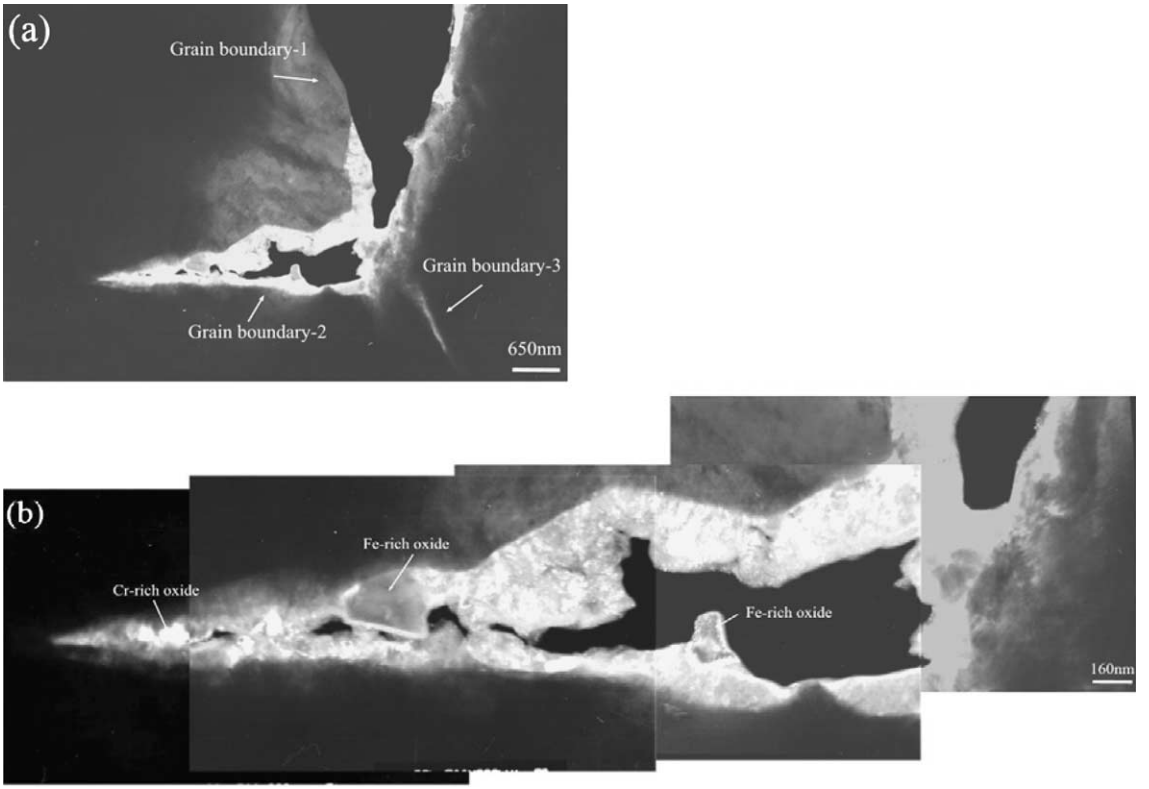

Fig. 8. (a) The dark field image and (b) the corresponding high-magnification image of the IGSCC crack tip shown in Fig. 5.

Table 3
EDS results at positions P1–9 labeled in Fig. 2(c)

	1	2	3	4	5	6	7	8	9
O	40.0	42.1	32.0	43.5	47.3	0	0	22.8	16.1
Cr	13.4	21.8	24.0	26.4	31.8	17.5	18.0	5.26	3.37
Fe	33.5	26.2	30.5	21.6	33.5	66.3	66.0	59.4	65.6
Ni	6.66	5.85	10.3	5.68	5.31	13.1	13.0	11.1	13.9

Unit: wt%.

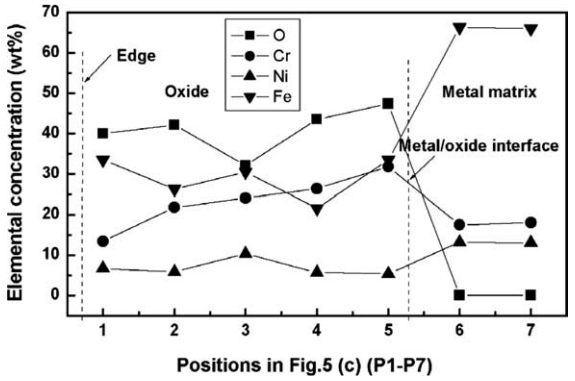

Fig. 9. EDS element profiles at the positions labeled in Fig. 5(c).

3.2. CT-1 specimen, high DO pure water

Fig. 12(a) shows a typical IGSCC crack containing many microcracks along a high angle grain boundary in CT-1 specimen after SSRT test in 288 °C pure water with high DO. The high-magnification images of crack tip A and ligament B in Fig. 12(a) shown in Fig. 12(b) and (c) reveal that some string type fracture bands are filled with oxide and carbon formed ahead of the crack tip A, and they are across the ligament B. The string type fracture band can provide a quick route for diffusion of oxygen and propagation of the main crack. Fig. 12(d) and (e) show high-magnification images of zone C in Fig. 12(a) and the corresponding diffraction pattern respectively. In Fig. 12(e) strong spots stand

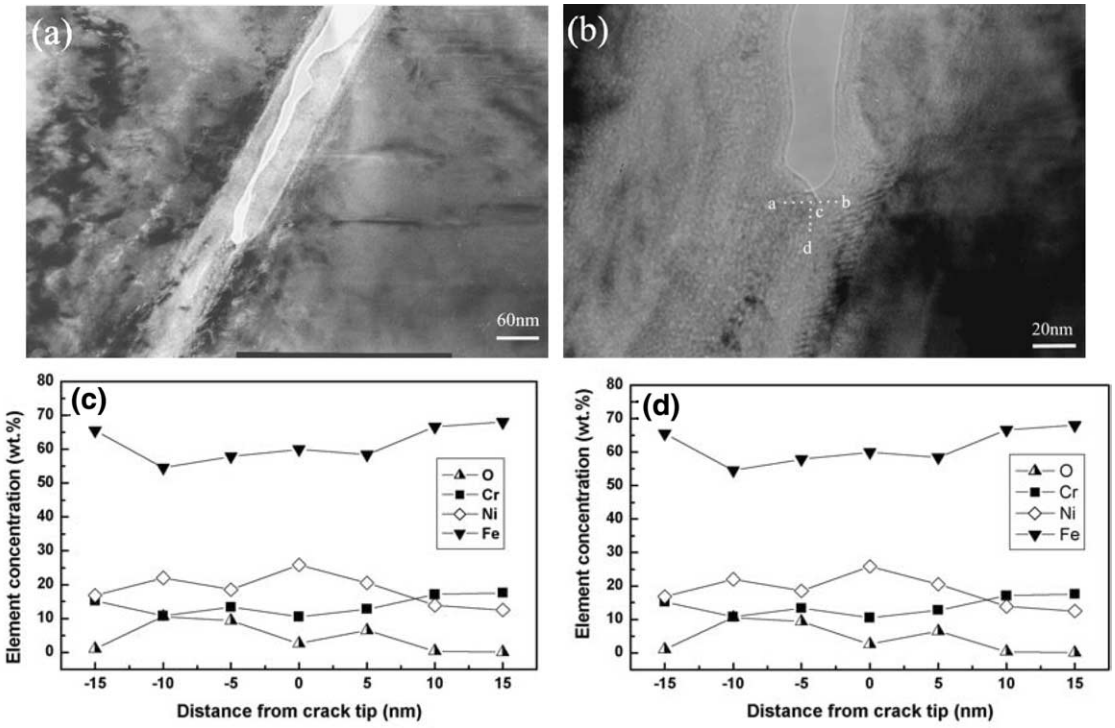

Fig. 10. (a) A transgranular SCC crack tip in CT-2 specimen tested in low DO water, and (b) the corresponding high-magnification image, as well as EDS profiles along (c) a–b and (d) c–d labeled in (b).

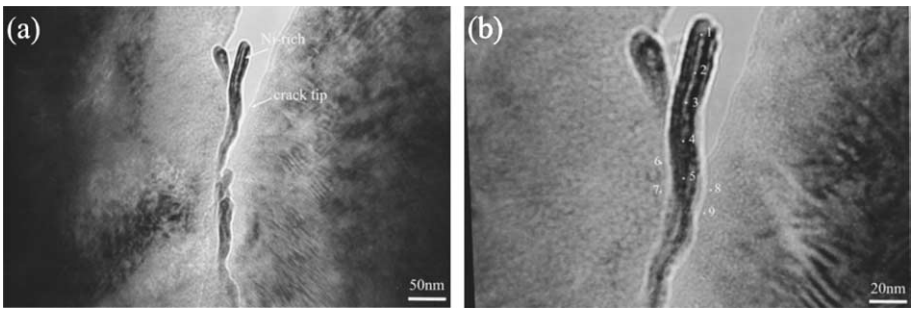

Fig. 11. (a) Another IGSCC crack tip in CT-2 specimen tested in low DO water and (b) the corresponding high-magnification image.

Table 4
EDS results at positions P1–9 labeled in Fig. 8(b)

	1	2	3	4	5	6	7	8	9
O	10.6	11.4	9.75	10.2	11.9	6.34	19.0	11.3	13.0
Cr	15.3	15.3	10.2	10.3	11.7	15.0	14.8	14.0	14.3
Fe	52.7	51.9	46.9	54.0	50.9	63.2	53.9	60.2	58.9
Ni	20.1	19.5	32.5	23.2	24.5	14.1	11.6	13.4	12.6

Unit: wt%.

for the austenitic stainless steel matrix, and weak spots for the oxide. For most positions within the grain boundary zone, the diffraction pattern exhibits only a series of rings, as shown in Fig. 12(f), when a fine probe

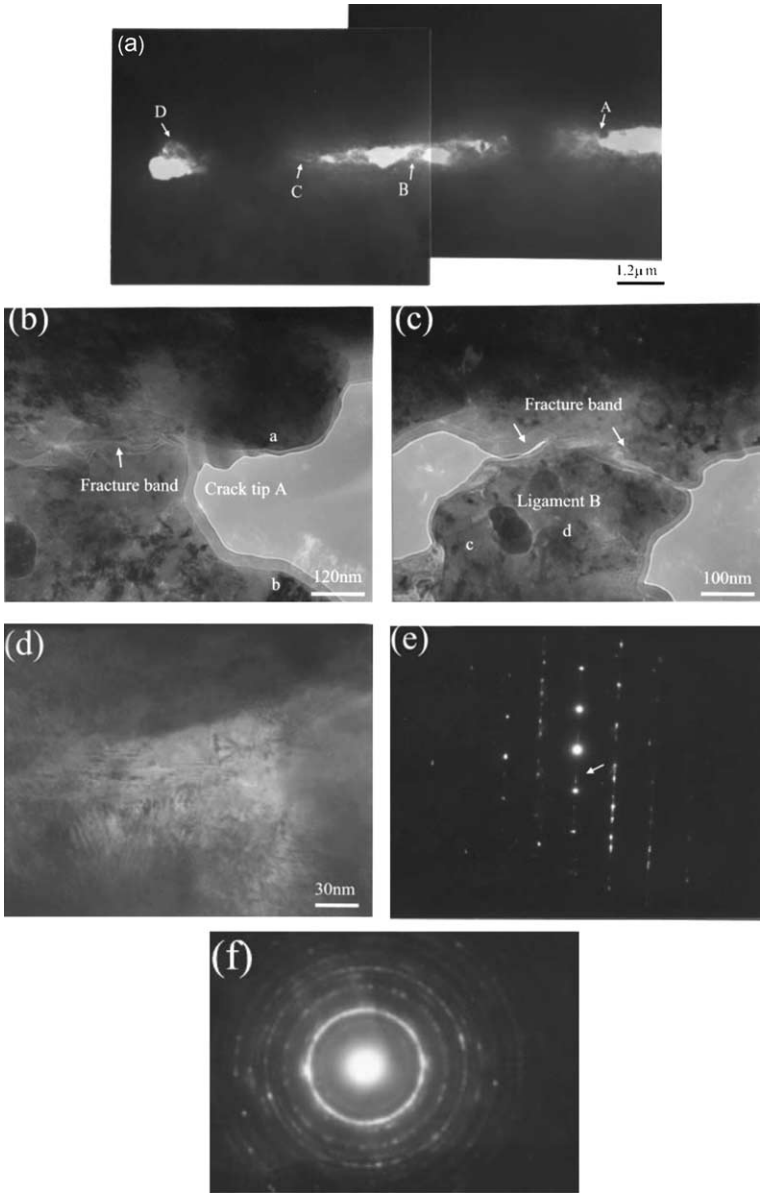

Fig. 12. (a) An IGSCC crack tip in CT-1 specimen tested in high DO water, and the corresponding high-magnification images of zones (b) A, (c) B (d) C, as well as the diffraction patterns taken from zones (e) C, and (f) B.

beam about 5–10 nm in diameter was used for diffraction. Using the diffraction spots of oxide the dark field image showing the existence of oxide can be obtained, as shown in Fig. 13(a) (the whole image) and Fig. 13(b) (the high-magnification image of circle zones labeled in Fig. 13(a)). From Fig. 13(b) the fine oxide crystal can be found to grow upward and distribute unevenly. The amount of oxide becomes less with penetration to deep grain boundary, which is obviously related to the oxygen diffusion process.

The further analyses on some oxides in Fig. 13 were conducted by the high-resolution lattice image. To perform this analysis the matrix grain on one side of the grain boundary was tilted to an exact (1 1 0) orientation. Fig. 14(a) and (b) show high resolution lattice images of oxides at positions a and b located at both sides of the crack tip A, respectively. The grain size of oxide is about 10–20 nm with its lattice space of (1 1 1) planes of about 0.5 nm. High-resolution lattice images shown in Fig. 14(c) and (d) were taken at the

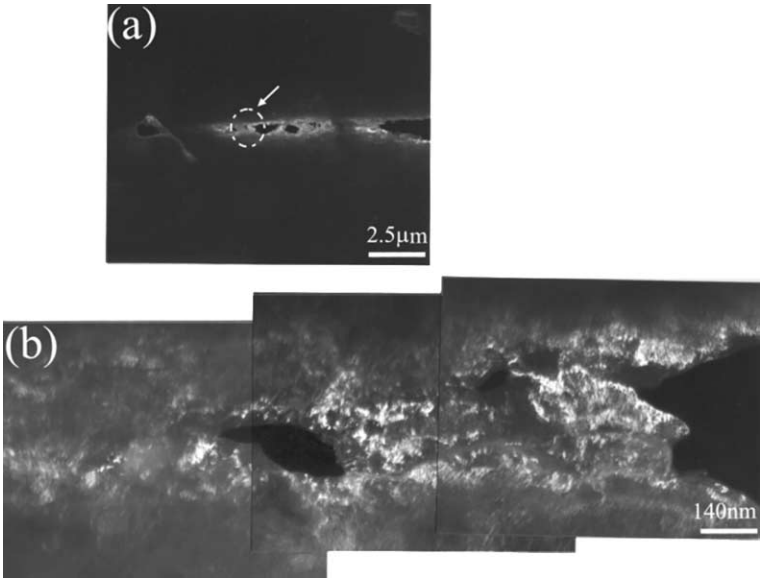

Fig. 13. (a) Dark field image of the IGSCC crack tip shown in Fig. 12(a), and (b) the corresponding high-magnification image of the circled zone labeled in Fig. 13(a).

positions c and d within the ligament B shown in Fig. 13(c). In Fig. 14(c) a moiré strip continuum can be obviously observed besides the fine matrix lattice strips on one side, indicating that a grain boundary exists in this position. By combining Fig. 14(c) with Fig. 12(c), it can be seen that the fracture band in Fig. 12(c) is not coincident with the grain boundary. In Fig. 14(d) the oxide lattice and some moiré strips due to lap of oxide and metal matrix are found. It can be concluded that the oxide in Fig. 13 are most likely $FeCr_2O_4$, Fe_2O_3 or Fe_3O_4 or their mixture according to the calculation using the diffraction ring and ASTM card. By combining with the high-resolution lattice image of oxide shown in Fig. 14 and some EDS results, the oxide shown in Fig. 12 is considered to be mixture of $FeCr_2O_4$ and Fe_3O_4.

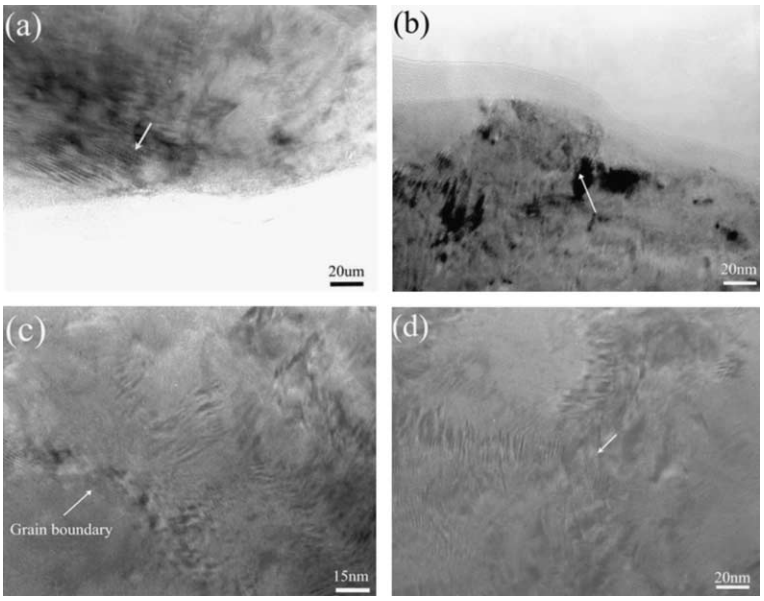

Fig. 14. High-resolution images at positions (a) a, (b) b in Fig. 12(b) and (c) c, (d) d in Fig. 12(c).

Another interesting phenomenon observed in Fig. 12(a) is the oxidation of silicon. Fig. 15(a) shows the high-magnification image of zone D shown in Fig. 12(a), where the bright area is silicon oxide, as indicated by the EDS analysis result shown in Fig. 16. The corresponding diffraction pattern shown in Fig. 15(b) indicates the silicon oxide here exhibits crystalline. The high-resolution lattice image of the silicon oxide shown

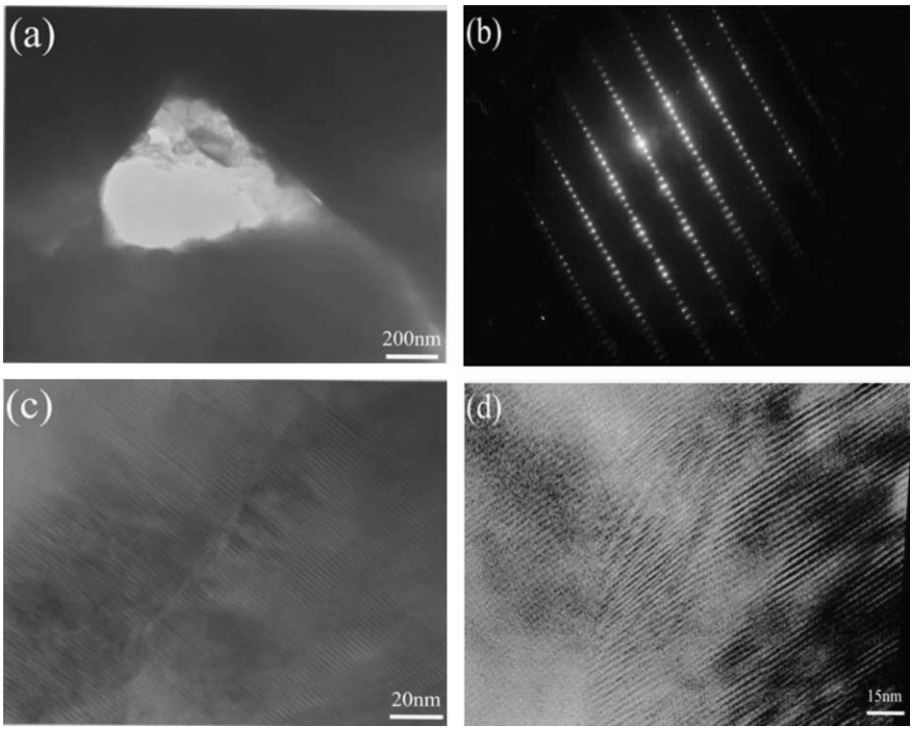

Fig. 15. (a) The high-magnification image of zone D shown in Fig. 12(a), and (b) the corresponding diffraction pattern, as well as high-resolution images of (c) silicon oxide and (d) a shear structure within it.

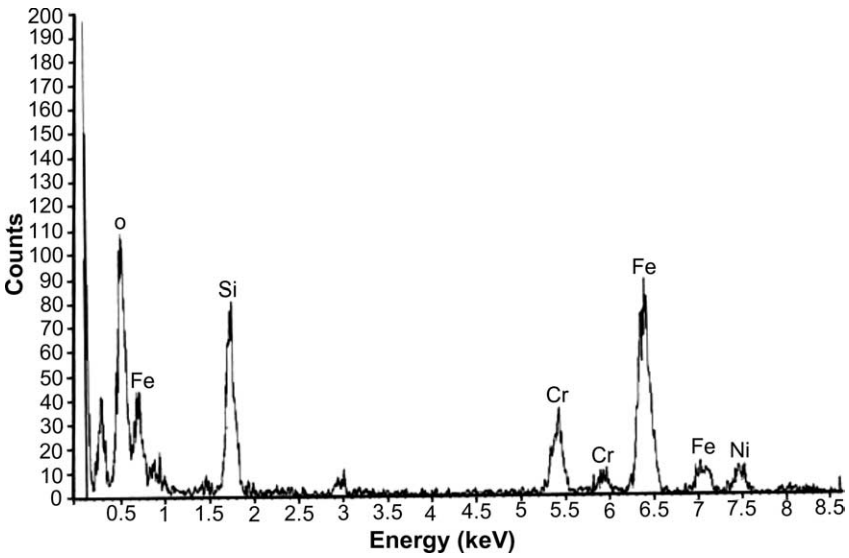

Fig. 16. An EDS spectrum of silicon oxide.

in Fig. 15(c) demonstrates that its lattice space is much larger, and a shear structure of silicon oxide because of lack of oxygen is found in Fig. 15(d). It can be seen from Fig. 12(a) that the microcrack produced inside silicon oxide is leading and has a large size, indicating that silicon may be oxidized more easily than Fe, Cr and Ni in stainless steel provided that silicon congregates at the grain boundary because of segregation, metallurgy and other factors.

A typical example of oxidation within a grain that leads to the formation of a transgranular SCC crack is provided in Fig. 17. Here A is an IGSCC crack; B, C and D are transgranular microcracks within a grain. High-magnification images of different positions, a, b and c in Fig. 17(a), are shown in Fig. 17(b)–(d), respectively. It can be seen that several string type oxide bands were formed ahead of the large microcrack. With further oxidation these string type oxide bands incorporate each other and become wider, as shown in Fig. 17(c). These oxide bands can be quick path for oxygen diffusion and crack propagation. It is noticed that within the oxides some microcracks were also found to nucleate, as

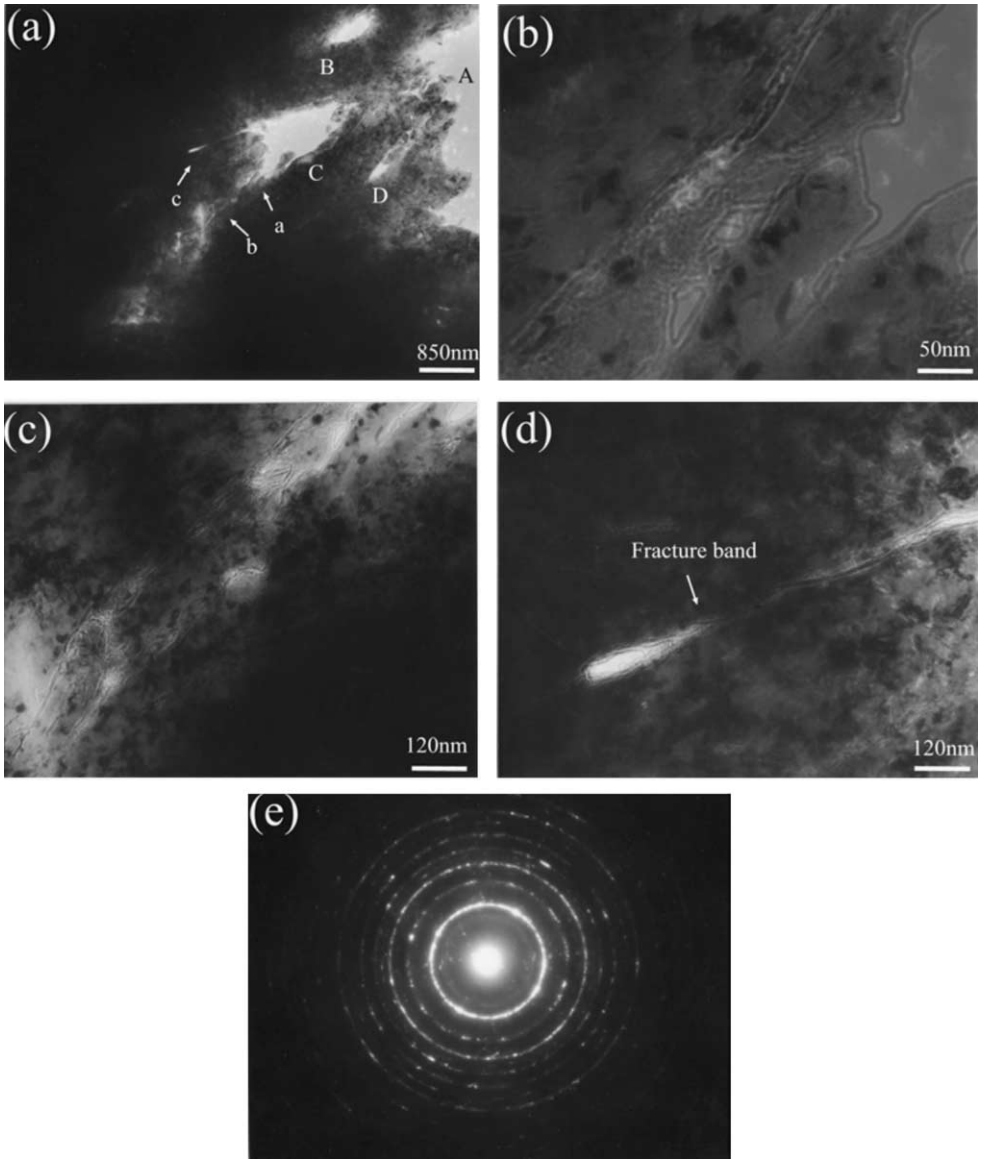

Fig. 17. (a) A transgranular SCC crack in CT-1 specimen tested in high DO water, and the corresponding high-magnification images of zones (b) a, (c) b and (d) c shown in (a), as well as (e) the diffraction pattern of oxide in (b).

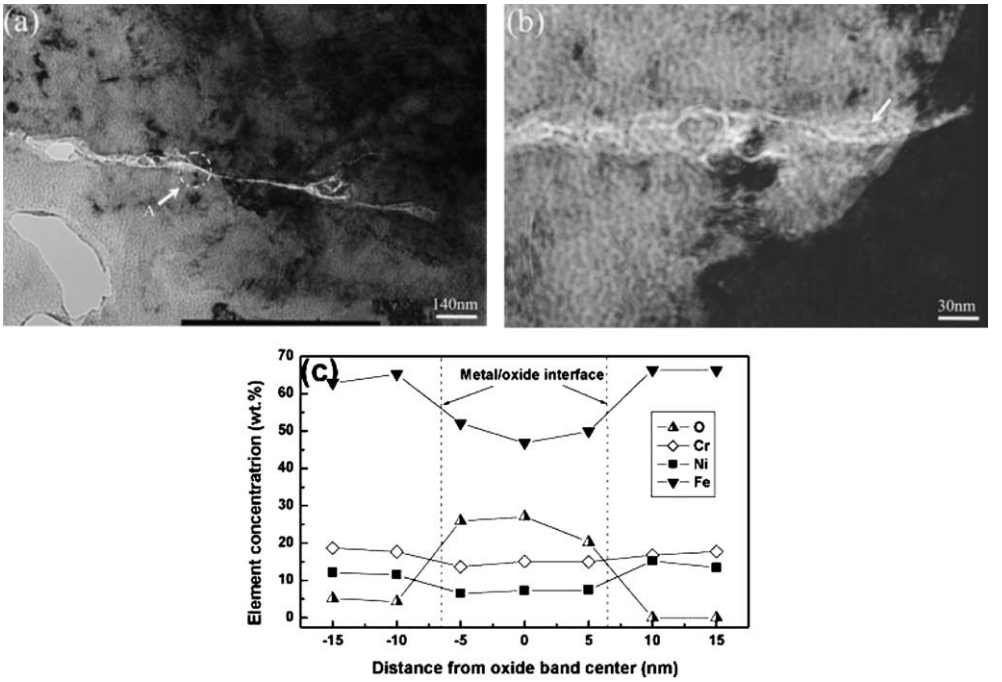

Fig. 18. (a) Another transgranular SCC crack in CT-1 specimen tested in high DO water, and (b) the corresponding high-magnification image of zone A, as well as (c) the EDS profile across oxide band at the position labeled in (b).

shown in Fig. 17(b)–(d). The corresponding diffraction pattern of oxide shown in Fig. 17(e) indicates that the oxide type is the same as that on grain boundary plane.

Fig. 18 shows another transgranular SCC crack (Fig. 18(a)) and the high-magnification image of the zone labeled A (Fig. 18(b)). An EDS analysis at the position labeled arrow across the oxide band was carried out, and its results are shown in Fig. 18(c), which also indicates that the oxide enrichment occurs within the oxide band.

4. Discussion

Extensive efforts have been made in the last decades to understand the crack tip oxidation mechanisms in stainless steel and other alloys in high temperature fatigue crack growth behavior experiments [15–17]. In general, oxygen short- and long-range diffusion processes are considered. In the short-range diffusion, rupture of the wedge-shape oxide intruding along the crack front can result in intergranular crack growth. In the long-range diffusion, oxygen penetrates materials of the crack tip along rapid diffusion paths such as slip planes and grain boundary, and the internal oxidation process takes place by way of internal oxide sites, cavity formation and/or solution segregation. Oxygen usually takes part in chemical reactions releasing known brittlement agents onto a grain boundary, resulting in intergranular crack growth [18]. Of course the oxidation mechanisms associated to the short- and long- range diffusions are not completely separated.

It is obvious that in the present study the following processes are related to the oxygen-induced SCC fracture [18].

(1) Oxygen from the crack surface diffuses along the grain boundaries and slip planes. Diffusion rate is temperature-dependent and susceptible to stress enhancement. Stress/strain assisted diffusion is important at the testing temperature of 288 °C.
(2) Oxygen reacts with the metallic species to form oxide. The oxides in different DO have different morphologies and microstructures.
(3) The main crack tip advances by linkage with microcracks formed within oxide under trapezoidal wave loading or SSRT.

It has been reported that the creep and hold-time fatigue crack propagation rate in many Ni base alloys are accelerated by up to orders of magnitude in air relative to vacuum environment, which is related to the oxygen brittlement of grain boundaries in the presence of tensile stress. This phenomenon is often referred as stress accelerated grain boundary oxidation (SAGBO) [19]. On the other hand, a research on hydrogen behavior ahead

of a crack tip has confirmed the stress/strain assisted diffusion [20]. In theory, Carranza et al. [18] has built an adaptive space–time finite element model for oxidation-driven fracture, in which stress-enhanced diffusive transport of reactive chemical species is used. Therefore, oxygen concentration resulted from the stress/strain concentration ahead of a crack tip can be expected. In other words, oxygen can penetrate deeply along a grain boundary by the strain/stress assisted diffusion. When oxygen partial pressure, PO_2, at some concentration points reaches a critical value for formation of oxide, the selective oxidation will take place there. Obviously, this process depends on the type of the grain boundary. For example, a special grain boundary such as a Σ3-twin grain boundary has a relatively compact atom arrangement, which increases the resistance of oxygen penetration, will result in a low PO_2 value. Therefore, the oxidation seldom takes place at twin grain boundaries, but mainly at random grain boundaries, as proved by the study of Thomas and Bruemmer [12]. When the PO_2 at the crack tip reaches the critical value required for formation of Cr oxide, the Cr_2O_3 type oxide first forms, as shown in Fig. 8(b) and in Ref. [12]. It can be explained by the lower PO_2 or bigger negative Gibbs free energy (ΔG^0) value for formation of Cr oxide compared with those of other oxides, which will be further described below. As a result, the Cr transports from surrounding area to the oxidation zone, leading to Cr depletion and Fe enrichment at surrounding area, followed by formation of Fe oxide there when PO_2 reaches the critical value for formation of Fe oxide. The rupture of the oxide produces a microcrack ahead of the crack tip. Thus, the repeat of the above process will result in formation of some microcracks ahead of the main crack tip, as indicated in Fig. 5(a) and Fig. 12(a). From Table 3 it can be found that the oxidation does not change Cr depletion adjacent to the grain boundary, implying that a long-range diffusion of Cr does not take place during oxidation. The Cr_2O_3 type oxide is thermodynamically stable and compact at high temperature, which can be considered to be protective layer that limits oxygen diffusion to the grain boundary, hence prevents grain boundary from further oxidation. However, under the effect of an external load and/or other factors, the microcracks formed along the grain boundary, for example positions C and D shown in Fig. 6, can destroy the integrality of Cr_2O_3 oxide film, and hence accelerate the oxygen diffusion along grain boundaries.

On the other hand, according to the ΔG^0–T map of some oxides, among the present elements Fe, Cr, Ni and Si, Si has the smallest critical PO_2 value required for formation of its oxide, and is the easiest to be oxidized. Cr is the next, and Ni is the most difficult. The study of Tian et al. also proves this oxidation sequence using the heat of formation of oxide [21]. Therefore, it can be expected that once Si congregates at grain boundary, it will be easily oxidized. The microcrack due to Si oxidation usually locates at the leading position, as shown in Fig. 12(a), which promotes nucleation and propagation of the SCC crack. Si enrichment due to neutron irradiation at grain boundaries has been reported by many researchers [22–24]. Some macroscopical tests carried out by Andresen et al. [6], Jacobs et al. [7] and others [8,9] also support oxidation mechanism of Si in EAC. For minor detrimental elements S and P, their critical PO_2 values are relatively high, therefore they are less possibly oxidized, resulting in their weak effects on EAC behavior.

Ni enrichment at crack tip is probably also related to stress/strain assisted diffusion, which is similar to the hydrogen and oxygen behaviors. In our experimental studies, Cr and Fe are oxidized and stabilized. But only Ni can move freely, and therefore congregates at the crack tip. Thomas and Bruemmer [13] also find the similar phenomena. Ni enrichment behavior during oxidation is also supported by the study of Tian et al. [21], in which oxygen-induced nickel segregation occurs in nitrogen plasma implanted AISI 304 stainless steel. No proof shows Ni has beneficial or detrimental effect on EAC [10]. However, Ni enrichment at the crack tip can keep the stability of austenitic phases and thus diminishes likelihood of stress-induced martensitic transformation due to stress concentration at crack tip.

A series of in situ TEM observations have shown that for ductile or brittle metal materials, dislocations firstly emit from the crack tip upon loading, and when emission and movement of the dislocations reach a critical level a microcrack nucleates [25,26]. However, after oxygen diffuses into grain boundary and oxide forms, the dislocations emitted from the crack tip will be restricted by oxide. As a result, the concentrated normal and shear strains ahead of the crack tip are restricted to the crack tip zone, hence a strain-localized band (deformation band) is formed, as shown in Fig. 19. The strain-localized bands have been found ahead of a crack tip in many deformed materials such as TiAl alloy [27,28] and in a fatigued copper single crystal [29]. In theory, Rice and Drucker [30] have proved that the strain-localized band usually occurs in the plane stress condition. In general, this deformation band usually forms accompanying with a large plastic deformation [31]. Thus, on one hand, the microcrack is preferential to initiate within the strain-localized band [29], and on the other hand, many defects such as dislocation within the strain-localized band provide a quick path for oxygen diffusion, leading to formation of oxide and oxidation-driven fracture. In addition, oxides formed adjacent to grain boundaries can hinder dislocation emission from the grain boundary, which will prevent the sliding and migration of the grain boundary, and therefore reduce the ability of relieving local stress built up during deformation, which finally leads to intergranular crack growth.

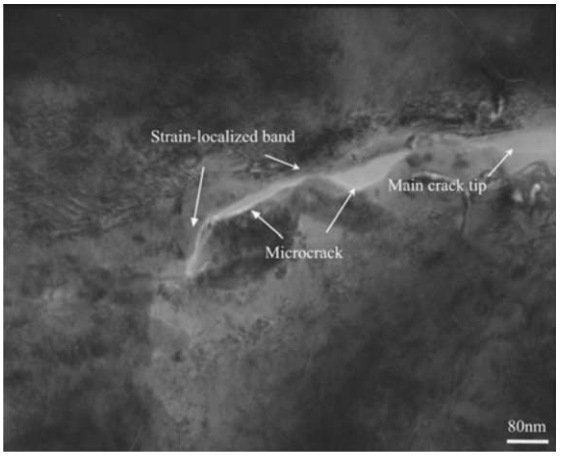

Fig. 19. Some strain-localized bands and microcracks ahead of an IGSCC crack tip in CT-1 specimen tested in high DO water.

The oxides at the crack tip also have similar structures as those at the surface. At low temperature of 288 °C Cr and Fe atoms diffuse in a short-range mode, thus separate Cr-rich and Fe-rich oxides with very fine grains can be formed at low DO. At high DO oxidation can occur further, leading to formation of mixed oxides consisting of $FeCr_2O_4$ and Fe_3O_4. The composition and structure of oxides are likely related to the loading modes. The SSRT is a continuously tension with a gradually increasing load, while for trapezoidal wave loading used in the current test, the load changes periodically from maximum to minimum (0.7 maximum) every 3 h. It is believed that for the current study, SSRT is more aggressive than the trapezoidal wave loading in promoting oxidation of crack tip and growth of SCC crack. However, the effect of loading modes on oxidation of crack tip is difficult to be verified. Many researchers have studied the surface oxide film in high temperature water, and a two-layer passive film is found to form on the surface of austenitic stainless steel after exposure to water with temperature above 250 °C [32,33]. The inner layer usually consists of a chromium-rich spinal $Ni_xCr_yFe_{3-x-y}O_4$ with high variable non-stoichiometric compositions such as Fe_2CrO_4, $FeCr_2O_4$ and $NiCrO_4$; while the out layer usually is ($Ni_xFe_{3-x}O_4$) in deoxygenated, hot and pressurized water, and Fe (III) oxide and Fe (III) oxyhydroxides such as Fe_2O_3 or FeOOH in oxygenated high temperature water.

The nucleation and growth of string type microcracks within the oxide are believed to be related to interaction between creep of oxide and external loading. The creep mechanism of oxide can be described by Nabarro-Herring [34] or Coble [35] mechanism, in which the creep rate is controlled by the interaction between diffusion and the grain boundary slip. It is presumed that at 288 °C the creep rate cannot catch up with the deformation rate produced by external loading, therefore an intergranular fracture of oxide takes place, resulting in nucleation and propagation of string type microcracks.

5. Conclusions

The oxidation behavior of SCC tips in heat-treated 304L stainless steel in high temperature oxygenated water with different DO was studied using ATEM. Several IGSCC and TGSCC cracks had been analyzed. The results indicated that:

(1) Oxygen played a key role in nucleation and propagation of SCC crack in heat-treated 304L stainless steel in high temperature oxygenated water. For the IGSCC crack, oxidation firstly occurred ahead of the SCC crack tip followed by propagation of the crack by linkage with microcracks within oxide on grain boundary plane.
(2) Oxidation along deformation bands and nucleation and growth of microcracks within oxide were important mechanisms of the TGSCC crack propagation.
(3) The oxides produced in different DO had different configurations and microstructures. Under Low DO condition separate oxides of Cr_2O_3 and Fe_3O_4 types were formed. On the other hand, high DO resulted in oxide mixture consisting of $FeCr_2O_4$ and Fe_3O_4 types.
(4) Si was preferentially oxidized, which promoted SCC crack propagation.
(5) Ni enrichment at some SCC crack tips was revealed.

References

[1] H.M. Chung, W.E. Ruther, J.E. Sanecki, A. Hins, N.J. Zaluzec, T.F. Kassner, J Nucl. Mater. 239 (1991) 61.
[2] O.K. Chopra, H.M. Chung, T.F. Kassner, J.H. Park, W.J. Shack, J. Zhang, F.W. Brust, P. Dong, Nucl. Eng. Des. 194 (1999) 205.
[3] J. Scott, J. Nucl. Mater. 211 (1994) 101.
[4] A. Jenssen, L.G. Ljungberg, J. Walmsley, S. Fisher, Corrosion 54 (1998) 48.
[5] M. Kodama, R. Katsura, J. Morisawa, et al., in: Proc. 7th Int. Symp. Environmental Degradation of Materials in Nuclear Power Systems – Water Reactors, Breckenridge, CO, USA, 7–10 August 1995, p. 1121.
[6] P.L. Andresen, F.P. Ford, S.M. Murphy, J.M. Perks, in: Proc. 4th Int. Symp. Environmental Degradation of Materials in Nuclear Power Systems – Water Reactors, Jekyll Island, GA, 6–10 August 1989, p. 1-83.
[7] A.J. Jacobs, R.E. Clausing, M.K. Miller, C. Shepherd, in: Proc. 4th Int. Symp. Environmental Degradation of

Materials in Nuclear Power Systems – Water Reactors, Jekyll Island, GA, 6–10 August 1989, p. 14-21.
[8] G.F. Li, Y. Kaneshima, T. Shoji, Corrosion Sci. 56 (6) (2000) 460.
[9] T. Yonezawa, K. Fujimoto, S. Nakata, K. Ajiki, K. Sakai, in: Proc. 8th Int. Symp. Environmental Degradation of Materials in Nuclear Power Systems – Water Reactors, La Grange Park, IL: ANS, 1997, p. 823.
[10] P.L. Andresen, C.L. Briant, Corrosion 45 (6) (1989) 448.
[11] C.L. Briant, P.L. Andresen, Metall. Trans. A 19A (1988) 495.
[12] L.E. Thomas, S.M. Bruemmer, Corrosion 56 (2000) 572.
[13] L.E. Thomas, S.M. Bruemmer, in: 11th Int. Conf. Environmental Degradation of Materials in Nuclear System, Stevenson, WA, 10–14 August 2003, p. 1049.
[14] L.E. Thomas, J.S. Vetrano, S.M. Bruemmer, in: 11th Int. Conf. Environmental Degradation of Materials in Nuclear System, Stevenson, WA, 10–14 August 2003, p. 1212.
[15] H. Ghonem, T. Nicholas, A. Pineau, Fatigue Fract. Mater. Struct. 16 (6) (1993) 577.
[16] S.G. Hong, S.B. Lee, Inter. J. Fatigue 26 (8) (2004) 899.
[17] A.A. Kaya, P. Krauklis, D.J. Young, Mater. Character. 49 (1) (2002) 11.
[18] F.L. Carranza, B. Fang, R.B. Haber, Comput. Methods Appl. Mech. Eng. 157 (1998) 399.
[19] J. Rosler, S. Muller, Scr. Mater. 40 (2) (1999) 257.
[20] R.M. Rieck, A. Atrens, I.O. Smith, Metall. Trans. 20A (1989) 889.
[21] X.B. Tian, Ricky K.Y. Fu, et al., Mater. Sci. Eng. A316 (2001) 200.
[22] S.M. Brummer, E.P. Simonen, P.M. Scott, P.L. Andresen, G.S. Was, J.L. Nelson, J. Nucl. Mater. 274 (1999) 299.
[23] T.R. Allen, J.T. Busby, G.S. Was, E.A. Kenik, J. Nucl. Mater. 255 (1998) 44.
[24] G.S. Was, T.R. Allen, J.J. Busby, J. Gan, D. Damcott, D. Carter, M. Atzmon, E.A. Kenik, J. Nucl. Mater. 270 (1999) 96.
[25] Q.Z. Zhen, W.Y. Chu, C.M. Hsiao, Acta Metall. Mater. 42 (1995) 4371.
[26] Q.Z. Zhen, K.W. Gao, W.Y. Chu, Y. Zhang, Fatigue Frac. Eng. Mater. Struc. 21 (1998) 1415.
[27] Z.W. Huang, P. Bowen, Scr. Mater. 45 (2001) 931.
[28] Y.H. Lu, Y.G. Zhang, L.J. Qiao, W.Y. Chu, Mater. Sci. Eng. A298 (2000) 91.
[29] Z.F. Zhang, Z.G. Wang, Z.M. Sun, Acta Mater. 49 (2001) 2875.
[30] J.R. Rice, D.C. Drucker, Int. J. Fract. Mech. 3 (1) (1967) 19.
[31] D. Kuhlmann-Wilsdorf, Acta Mater. 47 (1999) 1697.
[32] B. Stellwag, Corrosion Sci. 40 (23) (1998) 337.
[33] M. Cunha Belo Da, M. Walls, N.E. Hakiki, J. Corstet, E. Picquenard, G. Sagon, D. Noel, Corrosion Sci. 40 (1998) 447.
[34] C. Herring, J. Appl. Phys. 21 (1950) 437.
[35] R.L. Coble, J. Appl. Phys. 34 (1963) 1679.